Quantitative analysis of ultrathin doping layers in semiconductors using high-angle annular dark field images

C. P. LIU, A. R. PRESTON, C. B. BOOTHROYD & C. J. HUMPHREYS
Department of Materials Science and Metallurgy, University of Cambridge, Pembroke Street,
Cambridge CB2 3QZ, U.K.

Summary

It is well known that the high-angle annular dark field (HAADF) technique in scanning transmission electron microscopy is an incoherent imaging process in the lateral (*xy*) plane. However, as a consequence of the existence of partial coherence in the *z* direction, accurate quantitative interpretation of image intensity is difficult. The effects of coherence in the *z* direction can be reduced by increasing the inner collector angle of the annular detector so that the scattering from atoms in the *z* direction is essentially incoherent. We thus show that it is feasible to quantify the total As concentration of ultrathin $InAs_xP_{1-x}$ layers in InP in a simple but accurate way using a thickness integrated Bloch wave calculation including phonon scattering with a large inner collector angle of the annular detector of around 150 mrad. We compare the As composition derived from this approach with that from the Fresnel method and high resolution imaging. We also show that the non-linear variation of the HAADF intensity with thickness is consistent with our simpler simulations for such conditions. Therefore, this approach enables us easily and quickly to quantify compositions using HAADF images. The tetragonal distortion due to lattice mismatch is also shown to influence the contrast and has been included in the calculations.

Introduction

Doping layers in semiconductors that have widths of a few monolayers exhibit fascinating electrical and optical properties, as well as providing insight into impurity diffusion processes. Although the forms of the compositional profiles of such layers often control the electrical and optical properties of devices, very few techniques can be used to characterize them to monolayer accuracy. The high-angle annular dark field (HAADF) technique has achieved growing recognition as a powerful microanalytical tool in the scanning transmission electron microscope since for a sufficiently small probe the HAADF image shows highly localized scattering from each atomic column (Wang & Cowley, 1989; Pennycook & Jesson, 1991) and thus can provide a method for extracting chemical information at the atomic level.

The advantage of this technique is that it is an incoherent imaging process in the lateral plane. While the incoherent characteristics of high-angle scattering due to the dominance of phonon scattering and the absence of contrast reversals with increasing specimen thickness have been verified by both Bloch wave calculations (Pennycook *et al.*, 1990) and multislice calculations (Wang & Cowley, 1989; Kirkland *et al.*, 1987), most work has concentrated on qualitative structural characterization from HAADF images (Bollig *et al.*, 1996; Pennycook *et al.*, 1990). For quantitative composition analysis using HAADF, Pennycook *et al.* (1986) used a very weak diffraction condition to quantify the doping concentration of species such as As, Sb and Bi ions implanted into Si substrates, and interpreted their results using a variety of high-angle scattering cross-sections, claiming that the accuracy can be better than 20%. Recently, Anderson *et al.* (1997) have developed a method for the quantitative analysis of high resolution HAADF images using a multislice calculation incorporating thermal diffuse scattering and have extracted the compositional profile of a $GaAs/Al_{0.6}Ga_{0.4}As$ interface at near-atomic resolution. However, in the work of Pennycook *et al.* (1986), the amorphous-like doping layer in their sample makes it easier to tilt to a weakly diffracting condition than is the case for crystalline growth-interrupted doping layers such as the material examined here. In the work of Anderson *et al.* (1997), however, long calculation times are necessary. In this paper, we seek a quick and accurate method to analyse dopant concentrations quantitatively using HAADF.

Correspondence to: C. B. Boothroyd. Tel: + 44 (0)1223 334564; fax: + 44 (0)1223 334567; e-mail: cbb4@cam.ac.uk.
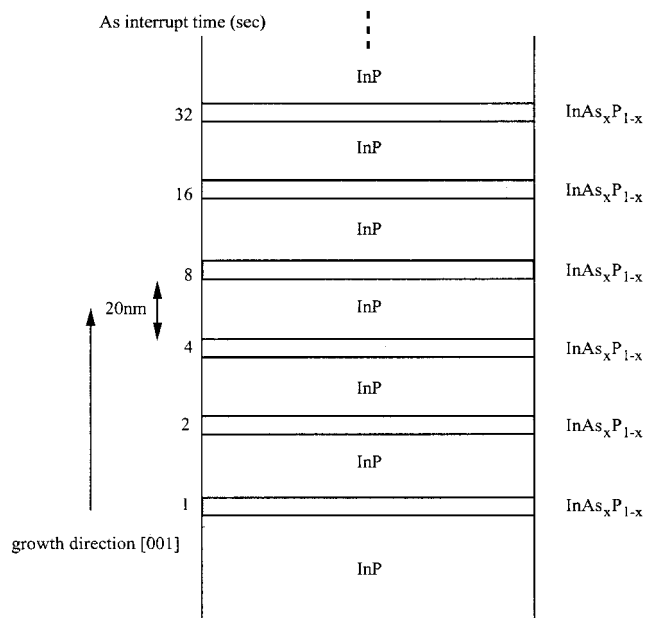
Fig. 1. Schematic diagram showing the structure of the specimen examined.

We use a much larger than normal inner angle for our annular detector, which enables us to assume that each atom scatters independently of its neighbours in both the *xy* plane and the *z* directions. We then use a Bloch wave calculation to calculate the intensity distribution in the sample and integrate this intensity along the beam direction to obtain the intensity on each atomic column. This can be used along with the scattering factors of the atoms in the column to estimate the scattered intensity on the annular detector. We show that it is feasible to quantify ultrathin layers in semiconductors in this simple but accurate way. We also show that the nonlinear variation of the HAADF intensity ratio with thickness is consistent with our simpler simulations for such conditions.

Experimental details

The layers examined here have already been examined qualitatively by Brown *et al.* (1993) and quantitatively by Liu *et al.* (1997), and are shown schematically in Fig. 1. Metal organic molecular beam epitaxy was used to grow a sequence of InP layers on (001) InP, between each of which the growth was interrupted in the presence of As_2 for periods of 1, 2, 4, 8, 16 or 32 s. This means that at the start of the growth interrupts, As_2 was switched on and In and P switched off. The reverse occurred at the end of the growth interrupts. The structure contained four such sequences of six $InAs_xP_{1-x}$ interrupts, with each interrupt separated from the next by an InP region of width approximately 20 nm. The substrate temperature was 500 °C. This model

structure is relevant to the technologically important InGaAsP-based multiquantum-well (MQW) layers in which the gas switching procedure typically leaves the InP surface exposed to As for several seconds in advance of InGaAs deposition. The consequent compositional spike at such an interface influences the operation of InGaAsP-based MQW lasers. In this paper, we concentrate on the characterization of one of the $InAs_xP_{1-x}$ layers in our model structure, corresponding to an interrupt time of 32 s. TEM specimens were prepared in the form of 90° wedges by cleaving on {110} planes. Thus areas of known specimen thickness could be examined and there were no amorphous surface layers due to ion beam thinning.

The material was examined using a VG HB501 STEM ($C_s = 3 \cdot 1$ mm), the annular detector of which was calibrated by taking diffraction patterns from a uniform region of InP substrate from the cleaved-wedge specimen. On account of the weak objective lens current caused by the geometry of the cleaved-wedge specimen in the microscope sample cartridge, the relation between scattering angle and distance from the centre of the diffraction pattern is approximately linear. Accordingly, the inner and outer collector angles of the annular detector used could be calibrated as about 150 and 300 mrad. The inner collector angle is greater than the 50–100 mrad normally used for HAADF imaging. The first order Laue zone for (001) InP occurs at 112 mrad and thus does not contribute to our images. Our probe diameter was about 0·7 nm so that atomic resolution was not attainable. However, low resolution images can still provide the total dopant concentration for the doped layers and have the advantage of providing a higher signal-to-noise ratio than atomic resolution images because a larger beam current can be used.

In order to measure the layer width of the ultrathin layers from HAADF images, great care was taken to ensure that the layers were exactly edge-on and the microscope was very close to focus, by selecting the closest to focus from a through-focal series. The imaging conditions were both at [001] zone axis and a few degrees off to a (020) systematic row condition. It can be seen qualitatively from the HAADF images in Fig. 2 that the bright contrast visible at the layers is consistent with As substituting for the lower atomic number P. In addition, no pronounced intensity oscillating thickness fringes can be observed on images either at or tilted away from [001], indicating that 1 s Bloch states dominate the contribution to the images. The layer width was measured to be $2 \cdot 1 \pm 0 \cdot 2$ nm for the layer arrowed in Fig. 2(b), which is a little wider than the previous result (1·8 nm) from the Fresnel technique (Liu *et al.*, 1997). The increased layer width is consistent with the expected broadening due to the convolution of the layer width with the probe size.

From the appearance of the high-angle dark field images, Figs 2(b) and (d), the contrast level is much higher when the
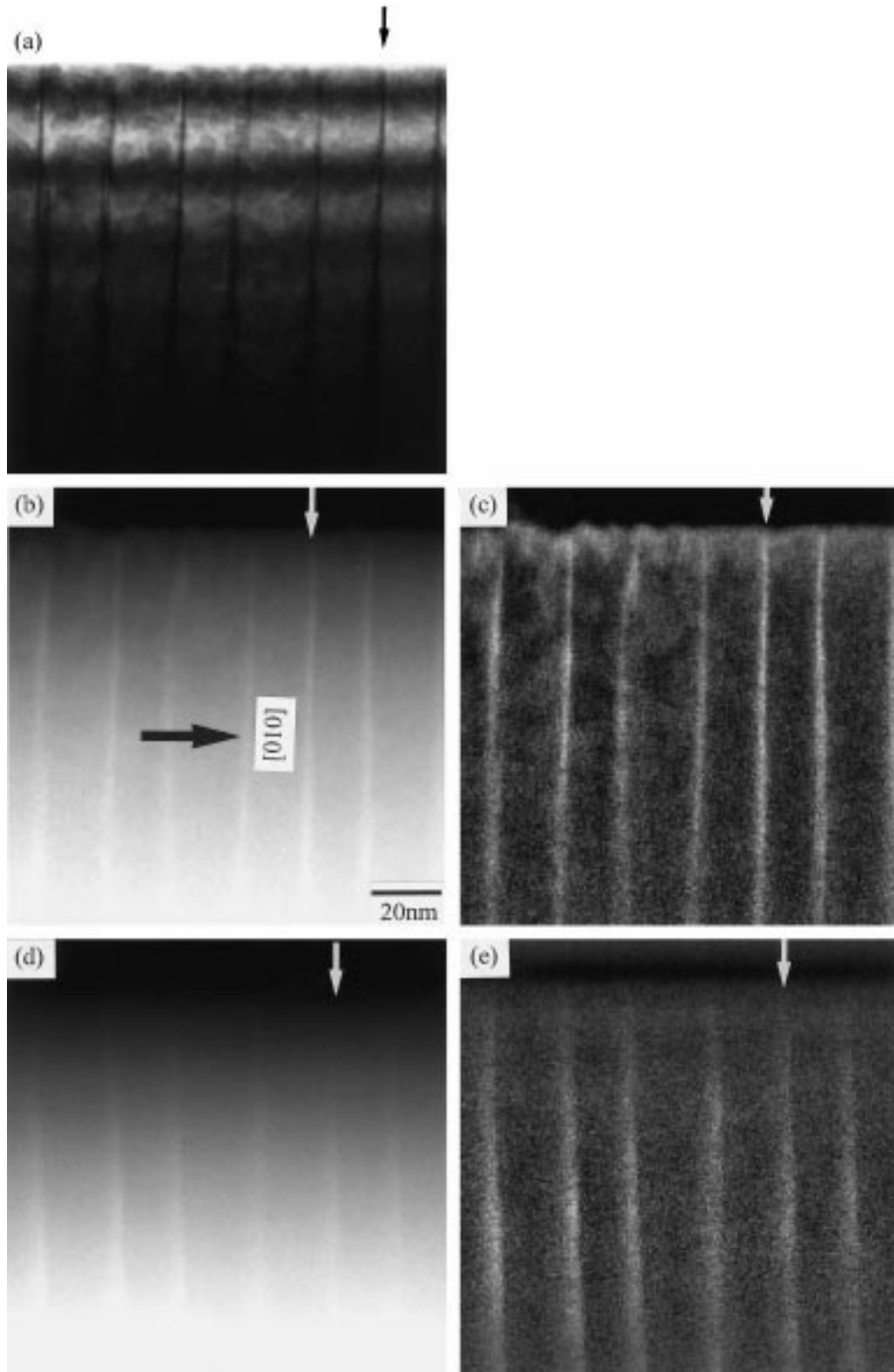
Fig. 2. Experimental 100 kV STEM images of As growth interrupts in a cleaved wedge of in InP. (a) bright field and (b) high-angle annular dark field images with an inner angle of 150 mrad and an outer angle of 300 mrad of InP along the [001] zone. (c) Image in (b) after high-pass filtering. (d) High-angle annular dark field image tilted a few degrees away from [001] along the (020) systematic row and high pass filtered in (e).
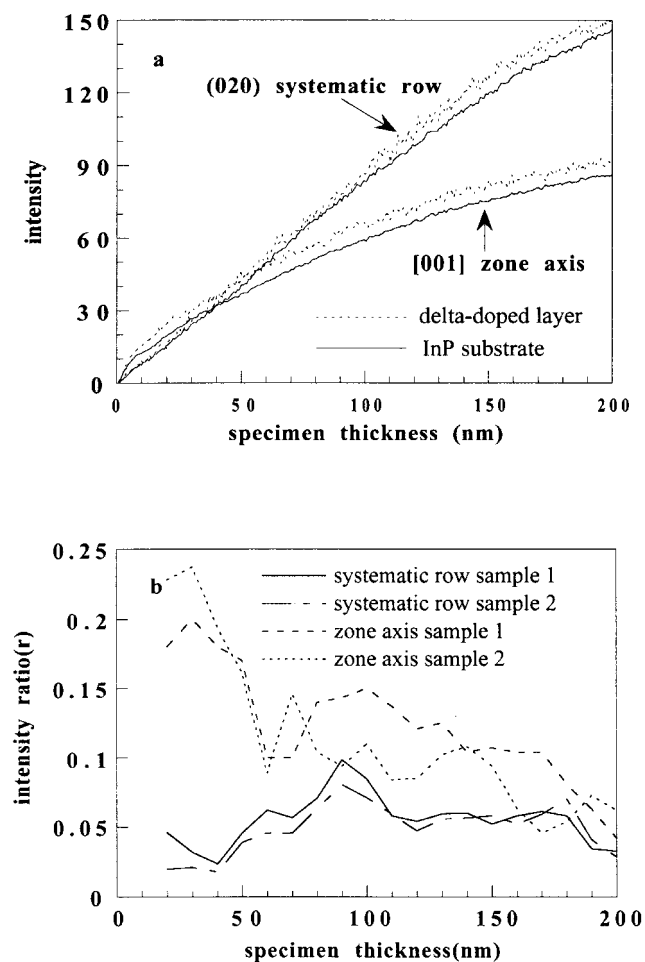
Fig. 3. (a) Typical HAADF intensity as a function of specimen thickness for the delta-doped layer and the InP substrate for two orientations plotted on the same intensity scale. (b) The intensity ratio (*r*) of the layers plotted as a function of thickness from two TEM specimens made from the same sample for two orientations.

beam is on the zone axis than when tilted a few degrees off, demonstrating that the HAADF image is sensitive to the crystal orientation as expected. The HAADF intensity as a function of specimen thickness for the delta-doped layer and InP substrate is shown in Fig. 3(a) for on and off zone axis condition. It is interesting to note that the HAADF intensity of both the As-containing layer and the InP substrate at the [001] zone axis is higher than at the (020) systematic row condition for thin regions but is attenuated faster and becomes weaker for thicknesses larger than about 40 nm. This indicates that at the [001] axis initially more intensity is scattered to high angles than at the (020) systematic row, but at larger thicknesses this is offset by the greater absorption of the incident electrons at the [001] zone axis. To investigate the As layer contrast quantitatively, we have extracted areas covering a thickness range of $\pm$ 5 nm from 20 to 200 nm across the highest As concentration layer and
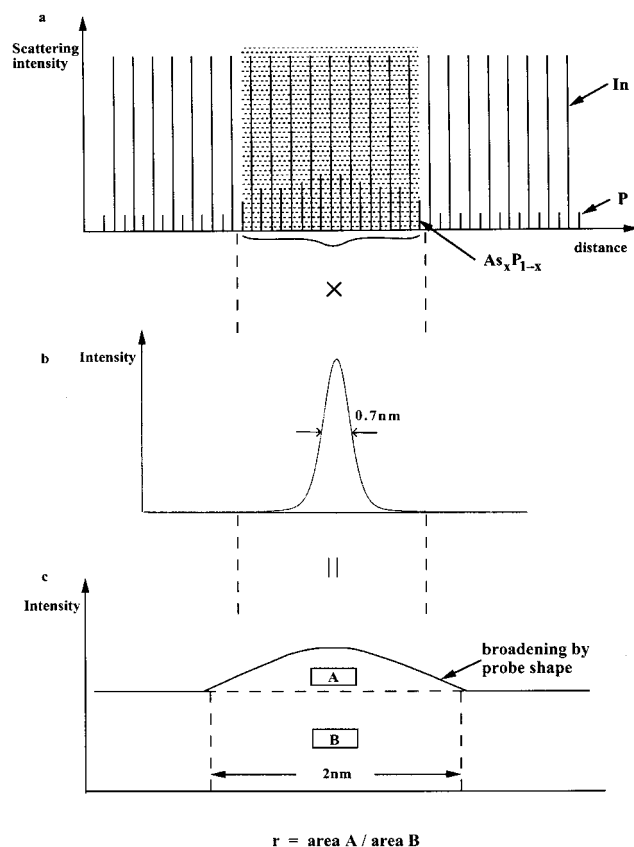

Fig. 4. (a) Simple atomistic model of an $InAs_xP_{1-x}$ layer in InP constructed for the specimen examined by convoluting a high-angle cross-section model with point atoms. (b) STEM probe intensity profile and (c) layer intensity after convolution showing the definition of the intensity ratio r = area A/area B.

projected these regions along the layers to give line traces. We then measure the 'intensity ratio', *r*, of the layer relative to the InP substrate by dividing the area under the layer (A in Fig. 4c) by the area under the InP for a width of 2 nm (B in Fig. 4c) for each thickness and show the intensity ratio as a function of thickness in Fig. 3(b). The area A was chosen as an approximate measure of the total As concentration in the layer independent of any broadening of the layer image relative to the brightness of the InP as measured by area B. If high-angle dark field images were totally incoherent and there was no channelling effect then the intensity ratio in Fig. 3(b) would be constant as a function of thickness and the same for images taken on and off the [001] zone, up to the thickness where multiple inelastic scattering events predominate. Instead, we see that the intensity ratio is much greater at [001] for low thickness than when tilted away from [001]. Although this discrepancy might be thought to be associated with the intrinsic inhomogeneity of the dopant distribution, the same trend was also observed in other samples with the same sequence of six doping layers. We are thus confident that this is a real effect and it

indicates that the conventional approach of assuming that HAADF contrast is proportional to Z^2 is invalid and that account must be taken of the dynamical scattering of the electron beam as it propagates through the crystal. In addition, the r-values for both on and off the zone axis tend to the same level at high thickness, consistent with inelastic scattering dominating at high thickness. This implies that in order to avoid too many inelastic events at high thickness, and a low signal-to-noise ratio and damage-induced strain due to specimen preparation at low thickness, the specimen thickness has to be chosen carefully.

Simulations

Our aim here is to measure the total dopant concentration of the As delta-doped layer by matching the intensity ratio measured experimentally with that from simulations. A full simulation of high-angle dark field intensities in STEM, taking into account all possible factors, typically requires a multislice calculation using a frozen phonon model for every position of the probe on the specimen, which is much too time consuming for a simple analysis. Thus here we use the simplified approach referred to in Section 1, where each atom is assumed to scatter incoherently with respect to its neighbours and in proportion to the beam intensity on that atom, and its contribution to the high-angle dark field image is assumed to be proportional to its scattering cross-section integrated over the angular range of the dark field detector. We calculate the electron intensity in the specimen as a function of position and depth with a simple Bloch wave calculation, and integrate the intensities on each atomic column in the beam direction. The assumption of incoherent scattering in the horizontal plane, i.e. that atoms separated horizontally act as independent scatterers, has been demonstrated to be correct for HAADF images (Jesson & Pennycook, 1993; Nellist & Pennycook, 1998). However, our approach also requires scattering to be incoherent in the z direction in order to allow us to sum the intensities scattered by each atom in a column, and we will now examine the validity of this assumption. Gibson & Howie (1978) have shown that the coherent scattering in hollow-cone illumination in the TEM decays laterally as a narrow damped Bessel function, and decays along the optical axis as a much more elongated shape. The typical elongated cigar shape of the coherence volume which defines the region around an atom which interferes coherently for high-angle scattering demonstrates the importance of coherence within each atomic column. Treacy & Gibson (1993) have also used hollow-cone illumination to examine the role of coherent scattering at high scattering angles as a function of thickness, both theoretically and experimentally. They point out that the inner angle of hollow-cone illumination can be used to control the scattering coherence and established an approximate criterion, which is given below,

for the critical angle above which the inner collector angle needs to be to avoid intracolumn coherence effects (the inner collection angle in HAADF STEM is related by reciprocity to the inner angle of hollow-cone illumination in TEM)

$$\alpha_c^{\text{intra}} = 2 \; \sin^{-1} \; (b\sqrt{3\lambda/8z}) \tag{1}$$

where z is the atomic spacing in the crystal along the atomic columns. Thus, for InP, which has a lattice parameter of 0·5868 nm, the critical angle along the [001] direction would be about 100 mrad at 100 kV and would be 115 mrad for the [011] zone axis. The critical angle becomes smaller than 100 mrad as the crystal is tilted off zone. The use of 150 mrad for the inner angle of the annular detector in our experiment is much larger than all the calculated critical angles. However, their treatment is based on kinematical scattering and the Einstein model, no correlation between atoms along a column, which potentially underestimates the coherence length along a column. Jesson & Pennycook (1995) have taken account of dynamical scattering as well as the phonon model and expressed the scattering from an individual atomic column in terms of an assembly of independent 'packets' of atoms. The atoms contained within a packet are partially coherent. Nevertheless, they also showed that the number of atoms in the packet depends on both the detector inner-angle and the Debye–Waller factor. For example, from their calculation, nine atoms have to be included in a packet for a 50–150 mrad ADF detector while only five atoms in a packet are required for a 100–150 mrad ADF detector. They concluded that the ADF intensity calculated from this approach will be deviated less than 20% from the incoherent model. Accordingly, the inner angle of 150 mrad for our experimental ADF detector which is much larger than normal inner angle makes the partial coherent scattering in the z direction insignificant and fully incoherent scattering is a good approximation for our specimen at [001] zone axis condition, while at (020) systematic row condition, the atoms along a column being displaced from it, the fully incoherent scattering can be applied.

Having now established that we can assume complete incoherence in the scattering from adjacent atoms both horizontally and vertically, we now have to calculate the electron intensity on each atomic site and the scattering cross-section of each atom. In incoherent theory (Kopf, 1981), images can be given as a convolution:

$$I^{\text{HA}} = O(R) \cdot P(R) \tag{2}$$

where I^{HA} is the HAADF intensity, $O(R)$ the object function and $P(R)$ the probe intensity profile as shown in Fig. 4. The object function is given below:

$$O(R) = \sum_i \sigma_i I(R - R_i) \tag{3}$$

where σ_i is the high-angle scattering cross-section for atom i

at position R_i and $I(R-R_i)$ is an intensity term taking account of the dynamical diffraction of the probe as it propagates through the crystal. Pennycook & Jesson (1991) have shown that $I(R-R_i)$ can be approximated as the thickness integration of the Bloch wave intensity distribution at the atomic sites as long as the scattering is an incoherent process. In our case this is justified because no thickness fringe oscillations are seen in our images (Figs 2 and 3a). The object function can be reasonably treated as a δ-function source of intensity localized at the atom position since the atomic potential for high-angle scattering is very much more localized than either the total absorptive potential or the elastic potential (Pennycook & Jesson, 1991). This characteristic in HAADF imaging of complete localization is also justified by the frozen-phonon model and multislice calculations of Wang & Cowley (1989).

It is not so obvious which high-angle cross-section is appropriate. While the atomic scattering amplitudes from Doyle & Turner (1968) and Rez *et al.* (1994) are most commonly used for conventional low-angle simulations, Zeitler & Olsen (1967) suggest that at the high-angles we are concerned with, the Born approximation is not suitable, particularly for heavier elements. Pennycook *et al.* (1986) concluded that Fleischmann's model (Fleischmann, 1960) fits best for the angle regime in their experimental cross-section ratios and Kirkland *et al.* (1987) also pointed out the invalidity of the Born approximation and suggested using the Moliere approximation (Moliere, 1947). Pennycook *et al.* (1986) have also carried out a comprehensive survey of all of the available models and have summarized them in terms of the product of the Rutherford differential cross-section $d\sigma_{\mathrm{Ruth}}/d\Omega$ with a screening function $q(\theta)$ as follows:

$$\frac{d\sigma}{d\Omega} = \frac{d\sigma_{\mathrm{Ruth}}}{d\Omega} q(\theta)$$

where

$$\frac{d\sigma_{\mathrm{Ruth}}}{d\Omega} = \left[\frac{m}{m_0}\right]^2 \frac{Z^2 \lambda^4}{4\pi^4 a_0^2 \theta^4}$$

and $q(\theta)$ are for different models, which are:

where $a_i = 0.1$, 0.55 and 0.35 and $b_i = 6.0$, 1.2 and 0.30 in the Moliere model. Accordingly, the cross-section for a particular atom can be derived by integrating each model over the range of solid angles corresponding to the high-angle detector. Figure 5(a) shows for an isolated Si atom at room temperature the atomic scattering amplitude from each model together with the scattering amplitude from Rez *et al.* (1994) for comparison, while Fig. 5(b) shows the total cross-sections and Fig. 5(c) the cross-section integrated over a narrow annulus up to 500 mrad at *s* for each model. As far as HAADF imaging is concerned, Fig. 5(a) represents the amplitude and Fig. 5(b) the intensity scattered to a given angle while Fig. 5(c) represents the total intensity collected by a high-angle detector with an inner angle of *s*. From these figures, the scattering predicted by the Rutherford model is always higher than the value of Rez *et al.* (1994) at low angles as a consequence of the absence of atomic electrons in the Rutherford model but, as expected, the two models tend to the same value above 150 mrad. Therefore, the high-angle partial cross-section for the annular detector of 150–300 mrad used here would be almost the same for both the Rutherford and the Rez models. For scattering angles around 100 mrad, the atomic scattering factors differ very much between all of the models. However, they eventually converge to similar values at very high-angles above 300 mrad. This indicates that the predicted HAADF intensity will become less model dependent as the inner collector angle of the annular detector is increased. Figure 6 shows the calculated high-angle cross-sections for In, As and P for each model and for an inner angle of 150 mrad and an outer angle of 300 mrad corresponding to the detector used in our experiment. We can see that all the models predict the expected behaviour that the high-angle cross-section increases with atomic number but that the values of the cross-sections differ by up to a factor of three between models.

In order to calculate the intensities on each atomic site as a function of the probe scanning direction, we use a Bloch wave calculation. Atomic scattering amplitudes are taken from Doyle & Turner (1968) with an absorption factor of 0.07 for all of the elements and Debye–Waller factors of
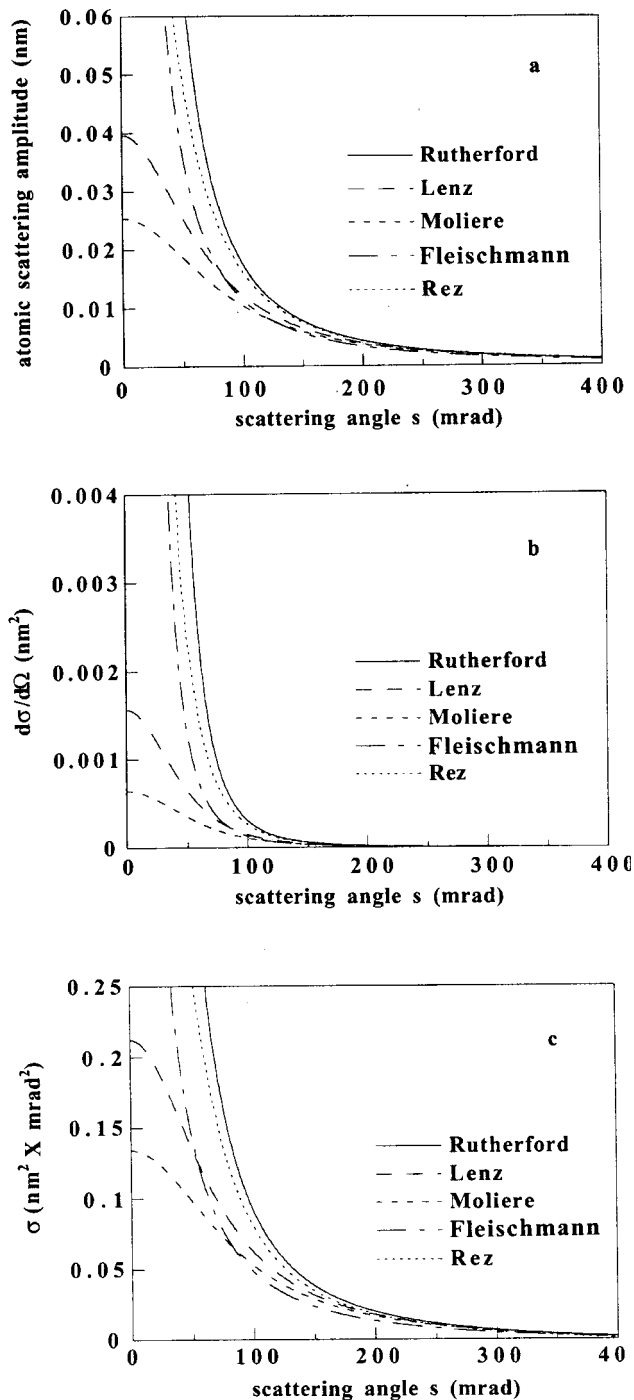
$$
\begin{cases}
1 & \text{Rutherford} \\[2ex]
\dfrac{\theta^4}{(\theta^2+\theta_0^2)^2}, \ \theta_0 = \dfrac{1.13 Z^{1/3}}{137\beta}, \ \text{where } \beta = v/c & \text{Lenz} \\[3ex]
\pi\theta^4\left[\displaystyle\sum_i \frac{a_i^2}{(\theta^2+b_i^2\theta_0^2)^2} + \sum_{i=2,3}\sum_{j<i} \frac{2a_i a_j}{(\theta^2+b_i^2\theta_0^2)(\theta^2+b_j^2\theta_0^2)}\right] & \text{Moliere} \\[3ex]
\dfrac{\theta^4}{(\theta^2+\theta_a^2)^2}, \ \theta_a^2 = \theta_0^2(1.13+3.76\alpha^2), \ \alpha = Z/137\beta & \text{Modifield Moliere} \\[3ex]
\dfrac{\theta}{\theta+\theta_a'}, \ \theta_a' = \theta_a e^{\frac{1}{2}} & \text{Fleischmann}
\end{cases}
\tag{4}
$$

Fig. 6. Calculated high-angle cross-sections of In, As and P for each model for an inner angle of 150 mrad and an outer angle of 300 mrad.

Fig. 5. (a) Atomic scattering factor, f, for an isolated Si atom at room temperature from different scattering models. (b) Total elastic cross-section $(= f^2)$ for an isolated Si atom at room temperature. (c) Total elastic cross-section integrated from the angle shown up to 500 mrad.

0·0091, 0·0058 and 0·0064 for In, P and As (Reid, 1983), respectively. (We appreciate the inconsistency of taking the same absorption factor but different DW factors for each element.) Figure 7(a) shows the general Bloch state
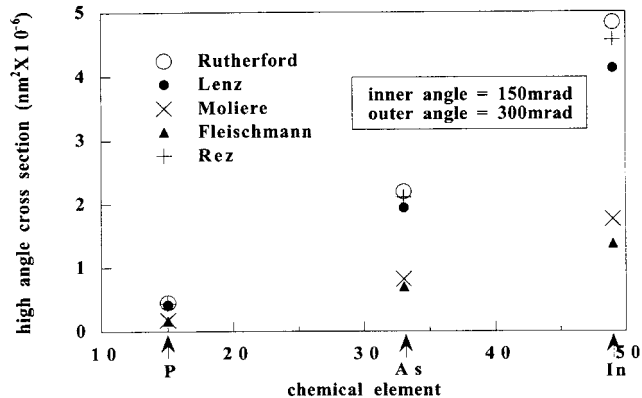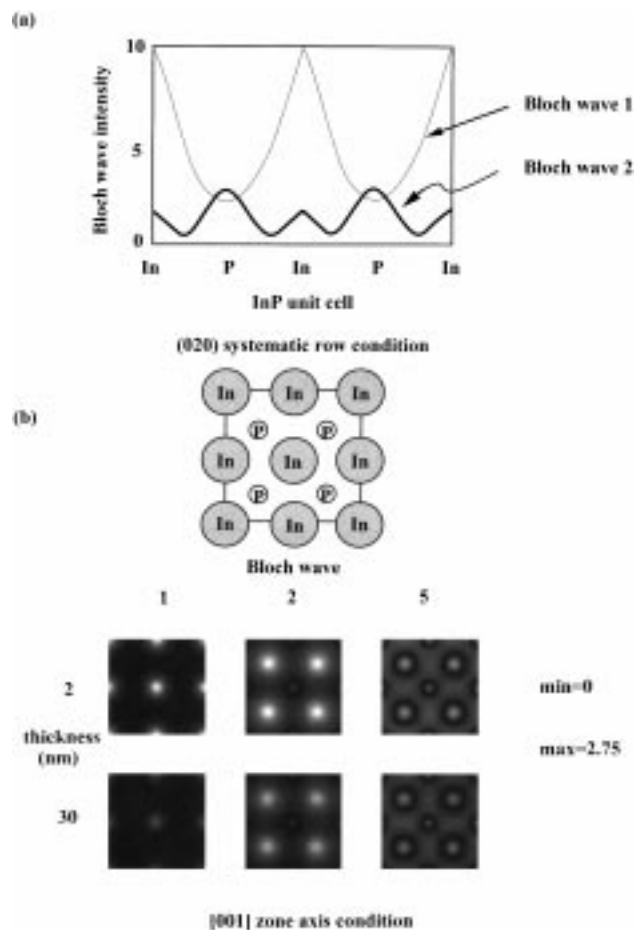

Fig. 7. The general Bloch state intensity distribution within a unit cell of InP (a) at an (020) systematic row for a thickness of 30 nm and (b) at the [001] zone axis for a thickness of 2 and 30 nm with a corresponding diagram of the unit cell plotted.
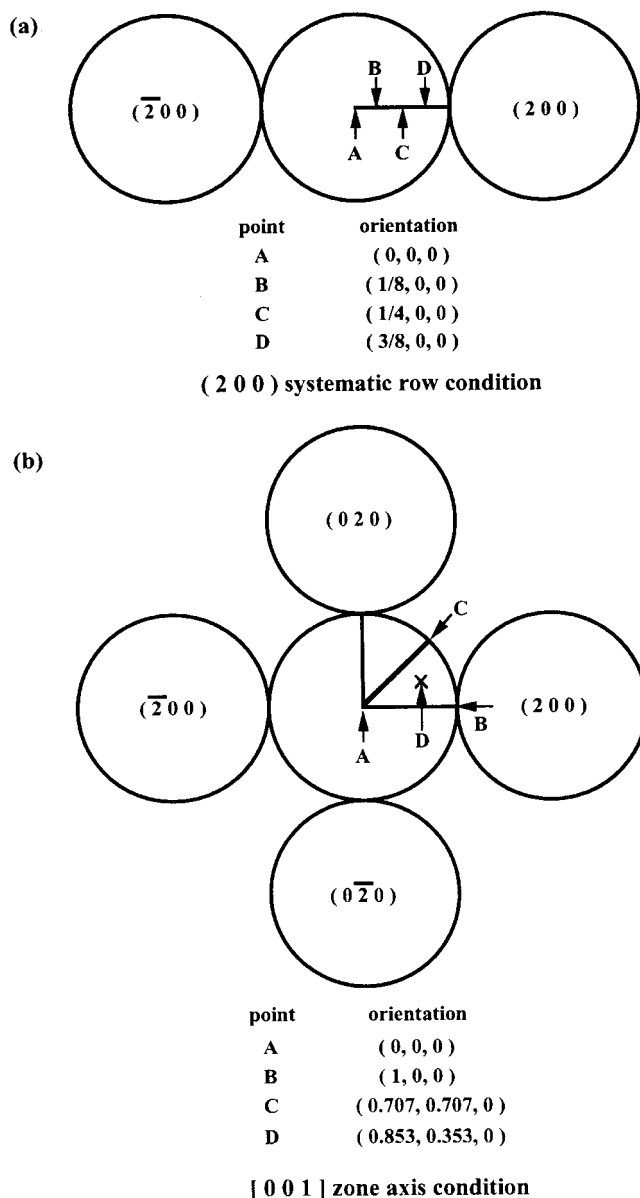
(a)

point	orientation
A	(0, 0, 0)
B	(1/8, 0, 0)
C	(1/4, 0, 0)
D	(3/8, 0, 0)

(2 0 0) systematic row condition

(b)

point	orientation
A	(0, 0, 0)
B	(1, 0, 0)
C	(0.707, 0.707, 0)
D	(0.853, 0.353, 0)

[0 0 1] zone axis condition

Fig. 8. Schematic diagram showing the four orientations used in the simulations within the incident convergent probe (a) (020) systematic row condition where the intensity is $I = \sqrt{16} \times A + \sqrt{15} \times B + \sqrt{12} \times C + \sqrt{7} \times D$ and (b) [001] zone axis condition where $I = A + 4B + 4C + 8D$.

intensity distribution within a unit cell of InP at an (020) systematic row for a thickness of 30 nm and Fig. 7(b) the Bloch wave intensity distribution at the [001] zone axis for a thickness of 2 and 30 nm with a corresponding diagram of the unit cell. Figure 7 shows that channelling is rather pronounced, which will in turn affect HAADF quantitative image analysis. It can be seen from Fig. 7 that Bloch wave 1 dominates away from [001] and contributes mostly on the In sites, although it is absorbed more than Bloch wave 2. At [001] Bloch wave 1 only dominates at very small thickness

Table 1. Intensity ratio (*r*) calculated for various probe profiles and dopant distribution models. All models contain the same amount of As.

Probe profile width (nm)	Dopant distribution model	Intensity ratio *r*
4.83	Spread diffusely over 10 monlayers	0.077
6.16	Spread diffusely over 10 monlayers	0.075
4.83	Abrupt 4 monolayers of As	0.079
4.83	Spread uniformly over 8 monlayers with 50% As for each monolayer	0.075

and attenuates rather quickly to almost zero at about 10 nm because of very strong absorption and then Bloch wave 2 takes over with the intensity mainly on the P sites. Therefore, the contrast for layers where As is substituting for P should be higher at the axial orientation due to channelling and this is consistent with our experimental observation. Moreover, absorption at [001], meaning that more electrons are scattered into the high-angle detector at small thicknesses, is the reason why the HAADF image intensity is higher at the (020) systematic row condition for large thicknesses, as observed in the experiment. Hillyard *et al.* (1993) also pointed out that the electron beam is channelled for long distances in low-Z elements such as Si or P while the beam travels only 100 Å before dechannelling in heavier elements such as In or Ge at the [001] zone axis. In order to achieve good accuracy in a reasonable time while calculating the Bloch wave intensity, great care has to be taken to determine how many beams need to be included in the calculations, especially for the zone axis condition. As seen in Fig. 7, there are three important Bloch waves which are Bloch waves 1, 2 and 5 for the [001] zone axis condition. However, to represent the excitation of Bloch wave 1 accurately, 150 beams must be included.

Given that As atoms are on group V sites, a thickness integration of the full Bloch state intensity with the composition varying from InP to InAs and the thickness from 10 to 100 nm for several representative orientations within the incident convergent probe both at [001] and away from [001] were calculated, where the unit cell for $InAs_xP_{1-x}$ ($x \neq 0$) was taken as tetragonally distorted based on conventional elasticity theory as a consequence of the lattice mismatch between InAs and InP (about 18·4%). The simulations can be performed now based on Eq. (2), as schematically drawn in Fig. 4, where the object function will be either a high-angle cross-section alone or a high-angle cross-section multiplied by the Bloch wave intensity. The probe function is shown in Fig. 4(b) and has a width of 0·7 nm for the condition used. This is slightly wider than the ideal probe size to allow for environmental disturbances, as with an ideal STEM probe shape high-resolution atomic
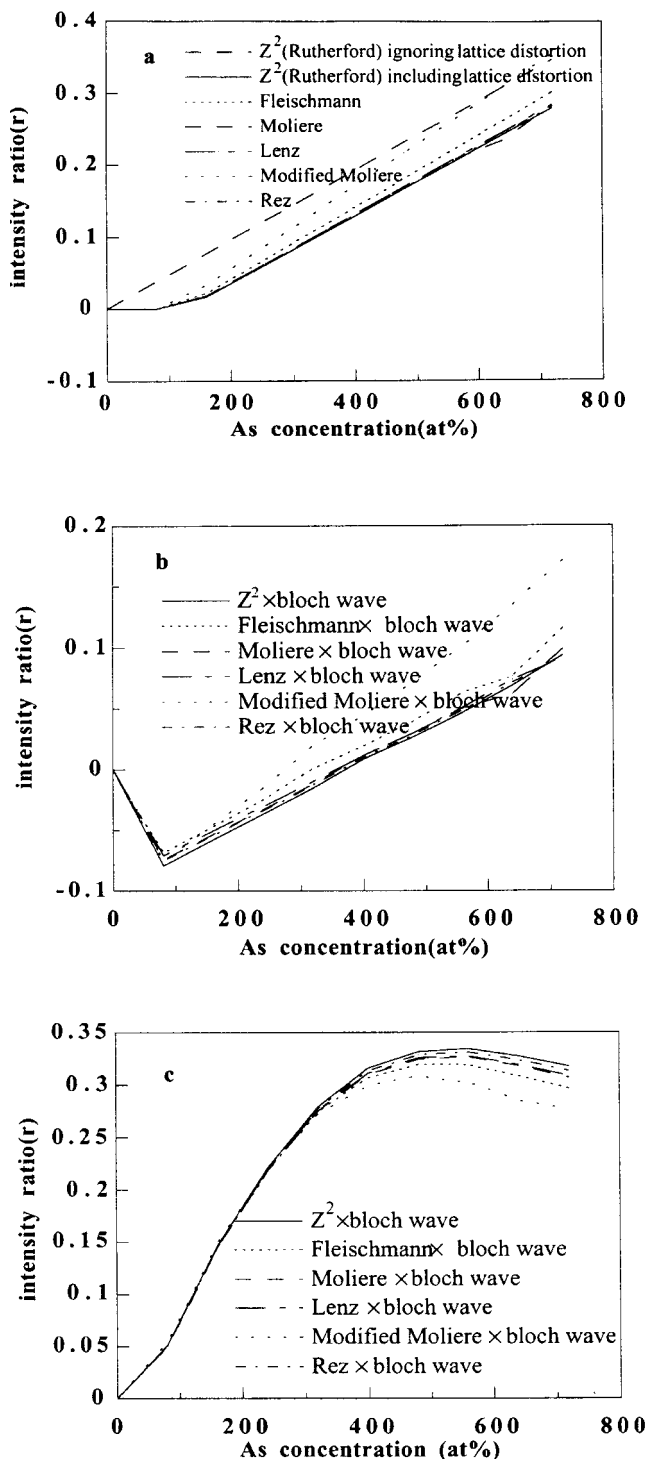
Fig. 9. The intensity ratio calculated as a function of As concentration for a thickness of 30 nm for a model considering (a) only the atomic cross-sections in the object function and (b) and (c) both the cross sections and the Bloch wave intensity terms for (b) the systematic row and (c) the zone axis conditions.

images should be just resolved. To calculate the intensity distribution, allowance has to be made for the convergence of the probe. Ideally, since the incident probe in this field-emission STEM is coherent, a full calculation for a coherent probe should be performed. However, the images are below lattice resolution, implying that the coherence is less important, and so for simplicity we have assumed the approximation of an incoherent probe and have picked points on the incident convergent probe and sum up the calculated intensity from all these orientations with an appropriate weighting factor. The orientations chosen are shown in Fig. 8.

Having now performed full Bloch wave calculations, the HAADF images can be calculated by convoluting the STEM probe function with the appropriate choice of delta functions at the atom sites to represent the appropriate high-angle cross-section and the Bloch wave intensity on the atomic sites. The model used in the calculations of total length of 25 InP monolayers is shown in Fig. 4, while the layer width of 1·8 nm and the dopant distribution were taken from the Fresnel analysis (Liu *et al.*, 1997). The tetragonal distortion due to the lattice mismatch is also crucial for HAADF images since it will change the local atomic density and hence the local scattering power and so it has also been taken into account in this object function using conventional elasticity theory. The intensity ratio calculated is proportional to the amount of As in the layer and is almost independent of how much the layer is spread due to the probe size. The effect of different As dopant profiles and different probe shapes on the intensity ratio is shown in Table 1. Here we see that the intensity ratio, *r*, is almost constant as both the dopant profiles and probe shapes are varied, indicating that it is a good measure of the total amount of As present in the layer regardless of its distribution or the microscope conditions. Accordingly, the theoretical intensity ratio, *r*, was calculated as a function of the As concentration for a model where the As is distributed evenly over 8 monolayers, for a number of cross-section models. Figure 9 shows the intensity ratio for a thickness of 30 nm for a model comprising only the cross-section term (i.e. assuming both In and P atomic columns have the same electron density) in (a) or a model including both the cross-sections and the Bloch wave intensity terms in the object function for the systematic row condition in (b) and for the zone axis condition in (c). Given that dynamical scattering is not included in Fig. 9(a), the intensity ratio is the same for all thicknesses and is sample orientation independent. The lattice distortion due to lattice mismatch is considered in all calculations except the top curve in (a). The intensity ratio for the top curve in (a) is always higher than those in the other curves in (a) since adding As causes an expansion and thus reduces the local scattering density. Comparing the intensity ratio when dynamical scattering is taken into account (Fig. 9b) with the intensity ratio when it is not allowed for (Fig. 9a), the intensity ratio in the former case is
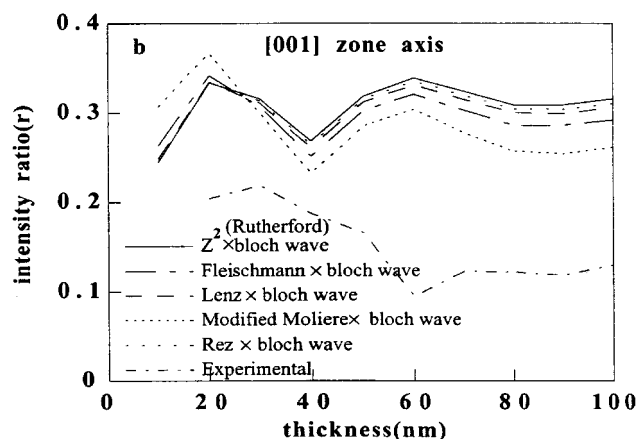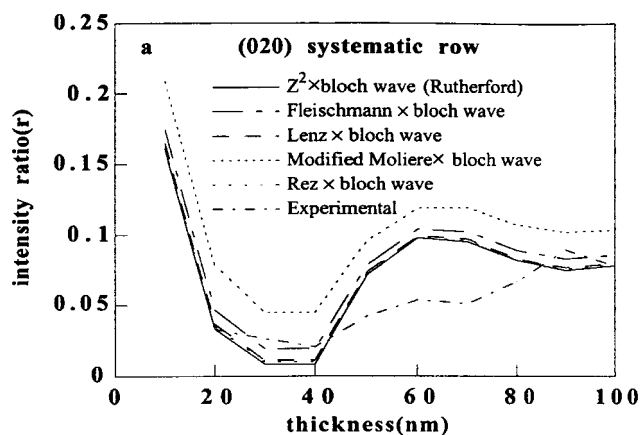
Fig. 11. The relative magnitude of intensity ratio, *r,* for the modified Moliere model with the Bloch intensity merely from the 1 s state compared with the Rutherford and modified Moliere models with the Bloch intensity from every Bloch state for the off-zone condition.

Fig. 10. The intensity ratio calculated as a function of thickness for an As concentration of 4 InAs MLs with the average of the two experimental results in Fig. 3 for comparison for (a) the systematic row and (b) the zone axis condition.

much lower and becomes negative due to the increased Bloch wave intensity at the In sites. For the zone axis condition shown in Fig. 9(c), more of the Bloch wave intensity is distributed into the group V sites so that the intensity ratio is much higher than that of the systematic row condition (Fig. 9b) and even higher than when dynamical scattering is ignored (Fig. 9a). This explains the layer contrast being higher in the zone axis condition. A consequence of the Bloch wave intensity dominating the intensity ratio is that there is almost no difference in the intensity ratio for the different cross-sectional models at concentrations below 4 InAs monolayers (MLs) in Fig. 9(c). Interestingly, it is also worth noting that the intensity ratio reaches maximum at a dopant concentration of 5 InAs MLs for the zone axis condition but remains fairly linear for the systematic row condition because the increase in the intensity ratio due to the amount of As compensates for
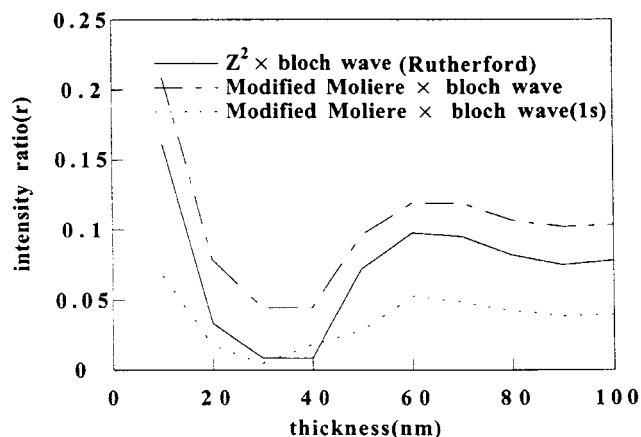
the loss of Bloch wave intensity on the group V sites. This indicates that if the dopant concentration is above a certain level, the layer contrast cannot be distinguished at the zone axis orientation but only at the systematic row orientation. The intensity ratio is then plotted as a function of thickness for an As concentration of 4 InAs MLs for the systematic row condition in Fig. 10(a) and for the zone axis condition in Fig. 10(b) with the average of the two experimental results in Fig. 3 for comparison. It can be seen that the variation of the intensity ratio with thickness exhibits Pendellosung fringes for both orientations. Hence, in principle, quantitative experimental data could be compared more reliably in thicker regions, although in practice thicker regions will suffer from more inelastic scattering which is difficult to account for in simulations.

Results and discussion

First of all, it is encouraging that the simulations of the intensity ratio as a function of thickness in Figs 10(a) and (b) do have the same general trend as the curve of the experimental results for both imaging conditions in the thinner regions. It can be seen that the Pendellosung behaviour in the experimental results arises from dynamical scattering and thus that any model that does not include dynamical scattering will fail to match the layer contrast for crystalline materials, even for systematic row conditions far from any major zone axes which would be expected to be the least dynamical. It can also be seen that the use of an annular detector with a large inner angle helps the quantitative analysis of ultrathin doping layers in semi-conductors.

For a first attempt, the intensity ratio for the layer with

the highest As concentration at a thickness of 30 nm is chosen for comparison, where the experimental values of intensity ratio are 0.027 ± 0.006 and 0.219 ± 0.02 for the systematic row and zone axis conditions, respectively. For the case when the beam is tilted far from the zone axis, although different cross-sectional models do give different results, all the models give values close to each other and within the experimental range, indicating that one benefit of using the large annular detector is a reduced dependence on the high-angle cross-sectional model. The As composition derived from HAADF using the modified Moliere model comes closest to the composition derived from the Fresnel method and other techniques (Liu *et al.*, 1997) of between 3.2 and 3.8 InAs MLs. However, when the beam is on the [001] zone axis, where the intensity ratio depends less on the cross-sectional model used, the As concentration is extrapolated to be 2.50 ± 0.3 InAs MLs, which is somewhat lower than previous results. The discrepancy is possibly attributable to the large change in the excitation of the Bloch waves for small tilts away from the zone axis and the residual partial coherence in the z direction as mentioned in the previous section. Thus, only a small misorientation of the specimen away from the zone axis is needed to produce a large change in the excitations of the In and P sites and thus make a large change in the layer contrast. It is for this reason that the most weakly excited condition is usually preferred for quantitative work since the images from such a condition are far less sensitive to misorientations.

The experimental intensity ratio, r, for the systematic row condition is obviously very low compared either to the model including only the Rutherford cross-section or to the model including dynamical scattering without the assumption of lattice distortion (top curve in Fig. 9a). This indicates that strain resulting from lattice mismatch also plays a significant role in reducing the layer contrast as well as the channelling effect. Regarding the channelling effect, calculations accounting for every Bloch state are essential for quantitative work rather than merely taking the predominant 1 s state (Pennycook & Jesson, 1991). Figure 11 shows the relative magnitude of the intensity ratio, r, for the modified Moliere model with the Bloch intensity from the 1 s state alone compared with the Rutherford and modified Moliere models with Bloch intensity from every Bloch state for the off-zone condition. Although the Pendellosung fringes are maintained, the difference in the intensity ratio between them is up to a factor of four.

Conclusions

Quantitative analysis of ultrathin doping layers in semiconductors using HAADF is feasible using an annular detector with a large inner angle to eliminate any coherent scattering in the Z direction. Therefore, the use of this large HAADF detector provides two advantages: firstly it makes image interpretation easier since simple Bloch wave simulations are sufficient rather than full multislice calculations and secondly the choice of the appropriate cross-sectional model for the high-angle regime is not so important when electrons are collected only at high scattering angles. However, full dynamical calculations including every Bloch state are essential. For our material, the strain resulting from lattice mismatch and the channelling effect appear to be the major factors in reducing the layer contrast experimentally when compared to a simple Z^2 assumption. The results for dopant concentration compared to simulations in this work shows that its accuracy can be better than 10%.

Acknowledgements

References

Anderson, S.C., Birkeland, C.R., Anstis, G.R. & Cockayne, D.J.H. (1997) An approach to quantitative compositional profiling at near-atomic resolution using high-angle annular dark field imaging. *Ultramicroscopy*, **69**, 83–103.

Bollig, B., Fischer, H.G. & Kubalek, E. (1996) Multislice simulation of high-resolution scanning-transmission electron-microscopy z-contrast images of semiconductor heterointerfaces. *Scanning*, **18**, 291–300.

Brown, P.D., Bithell, E.G., Humphreys, C.J., Skevington, P.J., Cannard, P.J. & Davies, G.J. (1993) The effect of growth interrupts on CBE grown InP. *Inst. Phys. Conf. Ser.* **134**, 373–376.

Doyle, P.A. & Turner, P.S. (1968) Relativistic Hartree Fock X-ray and electron scattering factors. *Acta Crystallogr.* **A24**, 390–397.

Fleischmann, H. (1960) Zur Kleinwinkeltheorie der Vielfachstreuung. *Z. Naturforsch.* **15a**, 1090–1096.

Gibson, J.M. & Howie, A. (1978) Investigation of local structure and composition in amorphous solids by high resolution electron microscopy. *Chem. Scripta*, **14**, 109–116.

Hillyard, S., Loane, R.F. & Silco, xJ. (1993) Annular dark-field imaging: resolution and thickness effects. *Ultramicroscopy*, **49**, 14–25.

Jesson, D.E. & Pennycook, S.J. (1993) Incoherent imaging of thin specimens using coherently scattered electrons. *Proc. R. Soc. London Ser. A*, **441**, 261–281.

Jesson, D.E. & Pennycook, S.J. (1995) Incoherent imaging of crystals using thermally scattered electrons. *Proc. R. Soc. London Ser. A*, **449**, 273–293.

Kirkland, E.J., Loane, R.F. & Silcox, J. (1987) Simulation of annular dark field stem images using a modified multislice method. *Ultramicroscopy*, **23**, 77–96.

Kopf, D.A. (1981) Measurement of the intensity distribution in a STEM probe. *Optik*, **59**, 89–110.

Liu, C.P., Dunin-Borkowski, R.E., Boothroyd, C.B., Brown, P.D. & Humphreys, C.J. (1997) Characterization of ultrathin doping layers in semiconductors. *Microsc. Microanal.* **3**, 352–363.

Moliere, G. (1947) Theorie der Streuung schneller geladener Teilchen I: Einzelstreuung am abgeschirmten Coulomb-feld. *Z. Naturforsch.* **2a,** 133–145.

Nellist, P.D. & Pennycook, S.J. (1998) Accurate structure determination from image reconstruction in ADF STEM. *J. Microsc.* **190**, 159–170.

Pennycook, S.J., Berger, S.D. & Culbertson, R.J. (1986) Elemental mapping with elastically scattered electrons. *J. Microsc.* **144**, 229–249.

Pennycook, S.J. & Jesson, D.E. (1990) High-resolution incoherent imaging of crystals. *Phys. Rev. Lett.* **64**, 938–941.

Pennycook, S.J. & Jesson, D.E. (1991) High-resolution Z-contrast imaging of crystals. *Ultramicroscopy,* **37**, 14–38.

Pennycook, S.J., Jesson, D.E.; & Chishalm, M.F. (1990) Atomic scale imaging of the structure and chemistry of semiconductor interface by Z contrast STEM. *SPIE*, **1284**, 182–194.

Reid, J.S. (1983) Debye–Waller factors of zinc-blende-structure materials – a lattice dynamical comparison. *Acta Crystallogr.* **A39,** 1–13.

Rez, D., Rez, P. & Grant, I.P. (1994) Dirac–Fock calculations of X-ray-scattering factors and contributions to the mean inner potential for electron-scattering. *Acta Crystallogr.* **A50,** 481–497.

Treacy, M.M.J. & Gibson, J.M. (1993) Coherence and multiple-scattering in Z-contrast images. *Ultramicroscopy,* **52,** 31–53.

Wang, Z.L. & Cowley, J.M. (1989) Simulating high-angle annular dark-field stem images including inelastic thermal diffuse-scattering. *Ultramicroscopy,* **31**, 437–454.

Zeitler, E. & Olsen, H. (1967) Complex scattering amplitudes in elastic electron scattering. *Phys. Rev.* **B162**, 1439–1447.